Morphological transitions and buckling characteristics in a nanoparticle-laden sessile droplet resting on a heated hydrophobic substrate

Lalit Bansal, Ankur Miglani, and Saptarshi Basu*
Department of Mechanical Engineering, Indian Institute of Science, Bangalore 560012, India
(Received 21 November 2015; revised manuscript received 15 January 2016; published 12 April 2016)

In this work, we have established the evaporation-liquid flow coupling mechanism by which sessile nanofluid droplets on a hydrophobic substrate evaporate and agglomerate to form unique morphological features under controlled external heating. It is well understood that evaporation coupled with internal liquid flow controls particle transport in a spatiotemporal sense. Flow characteristics inside the heated droplet are investigated and found to be driven by the buoyancy effects. Velocity magnitudes are observed to increase by an order at higher temperatures with similar looking flow profiles. The recirculating flow induced particle transport coupled with collision of particles and shear interaction between them leads to the formation of dome shaped viscoelastic shells of different dimensions depending on the surface temperature. These shells undergo sol-gel transition and subsequently undergo buckling instability leading to the formation of daughter cavities. With an increase in the surface temperature, droplets exhibit buckling from multiple sites over a larger sector in the top half of the droplet. Irrespective of the initial nanoparticle concentration and substrate temperature, growth of a daughter cavity (subsequent to buckling) inside the droplet is found to be controlled by the solvent evaporation rate from the droplet periphery and is shown to exhibit a universal trend.

DOI: 10.1103/PhysRevE.93.042605

I. INTRODUCTION

Evaporation of nanoparticle-laden droplets has been widely investigated to understand different phenomena ranging from coffee ring stains [1] to complicated starburst patterns during DNA deposition [2]. Sessile droplet evaporation is also important due to its implications in a plethora of applications such as surface patterning [3], inkjet printing [4,5], nanofabrication [6,7], and in self-assembly techniques [8–12]. The rate of evaporation is dependent on the contact angle of the sessile droplet which in turn affects the liquid flow profile. For instance, for droplets on hydrophilic substrates, evaporation can either proceed in constant contact radius (CCR) or constant contact angle (CCA) mode. In some cases, the droplets exhibit mixed evaporation in which both the contact angle as well as the contact radius decreases over the entire lifecycle. For droplets on hydrophilic substrates with pinned contact line (CCR), Deegan *et al.* [1] showed that the liquid flow field is directed radially outwards to compensate for solvent loss near the edge. This capillary flow is responsible for the formation of a coffee stain in pinned particle-laden droplets on hydrophilic substrate. However, droplets dispensed on hydrophobic substrates exhibit a very different flow pattern induced by Marangoni or buoyancy driven convections [13], mainly due to suppression of evaporation near the three phase contact line [14].

The flow structure, contact angle, and the evaporation dynamics are intricately coupled in sessile droplet vaporization. Hence it is intuitive that when sessile droplets are seeded with nano or microparticles, the flow dynamics in association with evaporation will be pivotal in preferential transport of particles at various sections of the droplet. Such transport mechanisms coupled with perikinetic (due to Brownian motion induced collision between particles or aggregates) and orthokinetic agglomeration (depends on the shear interaction between the particles) determine the final morphology of the dried precipitate. As an example, high contact angle particle-laden droplets undergo different morphological transformations (unlike a coffee ring) resulting in the formation of thin viscoelastic shells. This shell with progression of evaporation undergoes sol-gel transition (particles in the solution agglomerate to form a gelled skin surface) and buckles when the capillary pressure exceeds a critical buckling value [15–17]. This phenomenon of buckling in droplets is dependent on the rate of evaporation from the droplet surface as well as the contact angle and can be manipulated to control morphology of the final aggregate.

Rate of evaporation can be modified (suppressed or enhanced) either by varying the relative humidity around the droplet or by changing the droplet temperature, thereby increasing or decreasing saturation pressure. Forced convection can also enhance the evaporation rate around the droplet. Miglani *et al.* [15] increased the rate of evaporation by laser heating a levitated nanoparticle-laden droplet. They studied the buckling front kinetics and reported a deviation of droplet evaporation from the classical D^2 law during buckling. On the other hand, Evans *et al.* [18] suppressed solvent evaporation from the sessile droplet by placing similar droplets in a linear array. They observed preferential buckling from the locations where vaporization is suppressed. In the case of a sessile droplet, temperature can also be increased by heating the substrate. Chon *et al.* [19] used a microheater array (hydrophilic in nature) as a substrate for heating particle-laden droplet. However, they observed that higher substrate temperature had little effect on the final deposition pattern (coffee ring stains). Even though several numerical [20–22] and experimental studies [15,23–26] on particle deposition patterns during droplet vaporization have been reported in the literature, there is a dearth of information on the evaporation dynamics and subsequent pattern formation in high contact angle nanoparticle-laden droplets subject to controlled heating.

In the present work, rate of vaporization is increased by heating the hydrophobic substrate on which the nanofluid

*sbasu@mecheng.iisc.ernet.in

droplet is dispensed. The evaporative flux is significantly increased (by one order) as the substrate temperature is raised from the room temperature (25 °C) to 65 °C. In the case of a sessile droplet heated from below, the temperature is maximum at the base and it gradually decreases towards the apex. This variation in temperature along the droplet height affects the droplet evaporation and thereby the buckling kinetics (hence final deposition) as will be explained later. Dash *et al.* [13,27] theoretically (using the diffusion driven evaporation model) and experimentally analyzed the effect of substrate heating on the evaporative flux.

In our previous work [17], different stages of the lifecycle of a naturally evaporating sessile droplet (on a hydrophobic substrate) were studied. Buckling dynamics was observed for different nanoparticle concentrations and the cavity expansion was found to be sustained by the evaporation from the droplet surface. In this paper, the effect of substrate heating on the droplet evaporation, buckling front kinetics, and subsequent cavity formation are studied. We provide further proof for the cavity growth being driven by the solvent evaporation from the droplet surface which increases with increase in the substrate temperature.

II. METHODS AND MATERIALS

The experimental methodology involves deposition of a nanoparticle (NP) -laden droplet onto a heated hydrophobic substrate and imaging the droplet shrinkage and buckling dynamics using a high speed charge-coupled device (CCD) camera. The experimental setup is as shown in Fig. 1. A 3-μl droplet of nanosilica dispersion (Ludox TM40 from Sigma-Aldrich; average particle size of 25 ± 2 nm) is placed on a porous hydrophobic substrate (Teflon coated carbon paper of surface roughness $\sim 8\,\mu$m). The initial static contact angle is measured to be $\sim 125^\circ \pm 2^\circ$. The capillary length for a water droplet of equivalent volume is $l = \sqrt{\frac{\sigma}{\rho g}} \approx 2.7$ mm, which is larger than the initial droplet meridian radius ($R_i \approx 0.9$ mm). Thus, the gravitational forces are negligible and the droplet maintains its spherical geometry. The substrate is placed on an aluminum plate (2 mm thick) which is heated using a silicon tape heater (10 W). The heater is controlled using a PID (Proportional-Integral-Derivative) controller which ensures that a uniform substrate temperature (within ± 0.5 °C) is maintained. Experiments are conducted

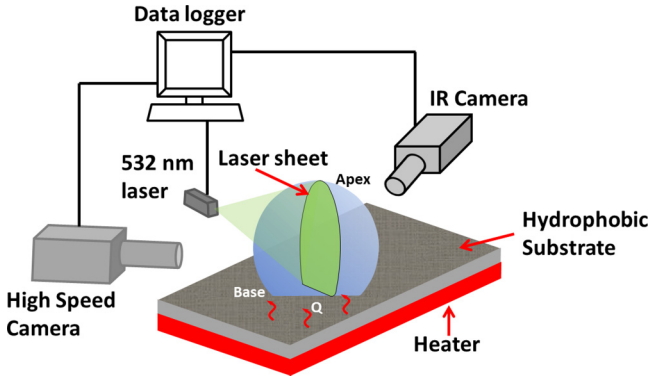

FIG. 1. Experimental setup.

for two initial particle loading rates (PLRs) of 20 and 40 wt % and at five different substrate temperatures: $T_s = 25$ °C, 30 °C, 45 °C, 55 °C, and 65 °C with relative humidity maintained at $45\% \pm 5\%$ (measured using a hygrometer TSP01 from Thorlabs). Henceforth, these cases at different temperatures and concentrations will be referred to as 20T30 (20 wt % at 30 °C), 40T45 (40 wt % at 45 °C), and so on. Buckling front kinetics is captured using a MotionScope NR3S1 camera fitted with a 1× Navitar lens (spatial resolution: 22 μm/pixel and temporal resolution: 100 ms). Spatiotemporal temperature variation across the droplet surface is measured using a FLIR SC5200 IR camera coupled with a lens (G3 Macro lens) at a spatial resolution of 5 μm/pixel (emissivity $\sim$0.95). The cases 20T30 and 40T30 are referred to as natural drying cases (along with 20T25 and 40T25) since not much change is observed in the droplet morphology when the T_s is increased from the ambient (25 °C) to 30 °C while other cases (at higher T_s) are referred to as heated substrate cases. Multiple experimental runs (five runs) were conducted for each condition (given substrate temperature and initial concentration) to assure repeatability. Nevertheless, data across all experimental runs have been reported in the figures as explained in the later sections.

III. GLOBAL OBSERVATIONS

In this section, we provide different observations regarding changes in the droplet morphology (as shown in Figs. 2 and 3) induced by the heating of the substrate at various temperatures (see previous section). The temperature along the height of the droplet (from bottom to top) shows a steady decrease (IR images in Fig. 2) for all heated cases. The maximum values of the temperature differential ($\Delta T = T_{\text{base}} - T_{\text{apex}}$) at different T_S are tabulated in Table I. ΔT exhibits higher values (1 °C−13 °C) with increase in substrate temperature. The droplets undergo evaporation in CCR mode (variation in contact radius is limited to 10%−15% of the initial value) at all substrate temperatures and nanoparticle concentrations. Irrespective of the substrate temperature, the droplet exhibits similar distinct phases (Figs. 2 and 3) in its lifecycle like natural drying, i.e., (1) initial shrinkage, (2) particle deposition on the droplet periphery and base resulting in the formation of a porous shell (dome shaped structure), (3) buckling of the porous shell in the top sector and subsequent rupturing, and (4) cavity growth inside the droplet leading to final aggregate. Even though the phases are similar, at higher temperatures, various changes in the droplet morphology are observed (as can be seen from Figs. 2 and 3) compared to the natural drying scenario. These changes are (1) increase in the base agglomeration height [$\frac{h_{a,65\,^\circ\text{C}}}{h_{a,25\,^\circ\text{C}}} = 2.43$ as shown in Fig. 4(c)]; (2) increase in droplet height [$\frac{h_{65\,^\circ\text{C}}}{h_{25\,^\circ\text{C}}} = 1.4$, in Fig. 4(b)]; and (3) decrease in time delay to buckling onset as compared to natural drying [Fig. 4(a)] leading to earlier shell (dome) formation. In addition, for initial PLR of 40 wt %, there is an increase in the number of buckling sites (shown by the white arrows in Figs. 2 and 3) with only one of them undergoing rupture (shown by the red arrows in Figs. 2 and 3). However, when the initial nanoparticle loading is decreased to 20 wt %, the droplet buckling and subsequent rupturing occur from a single

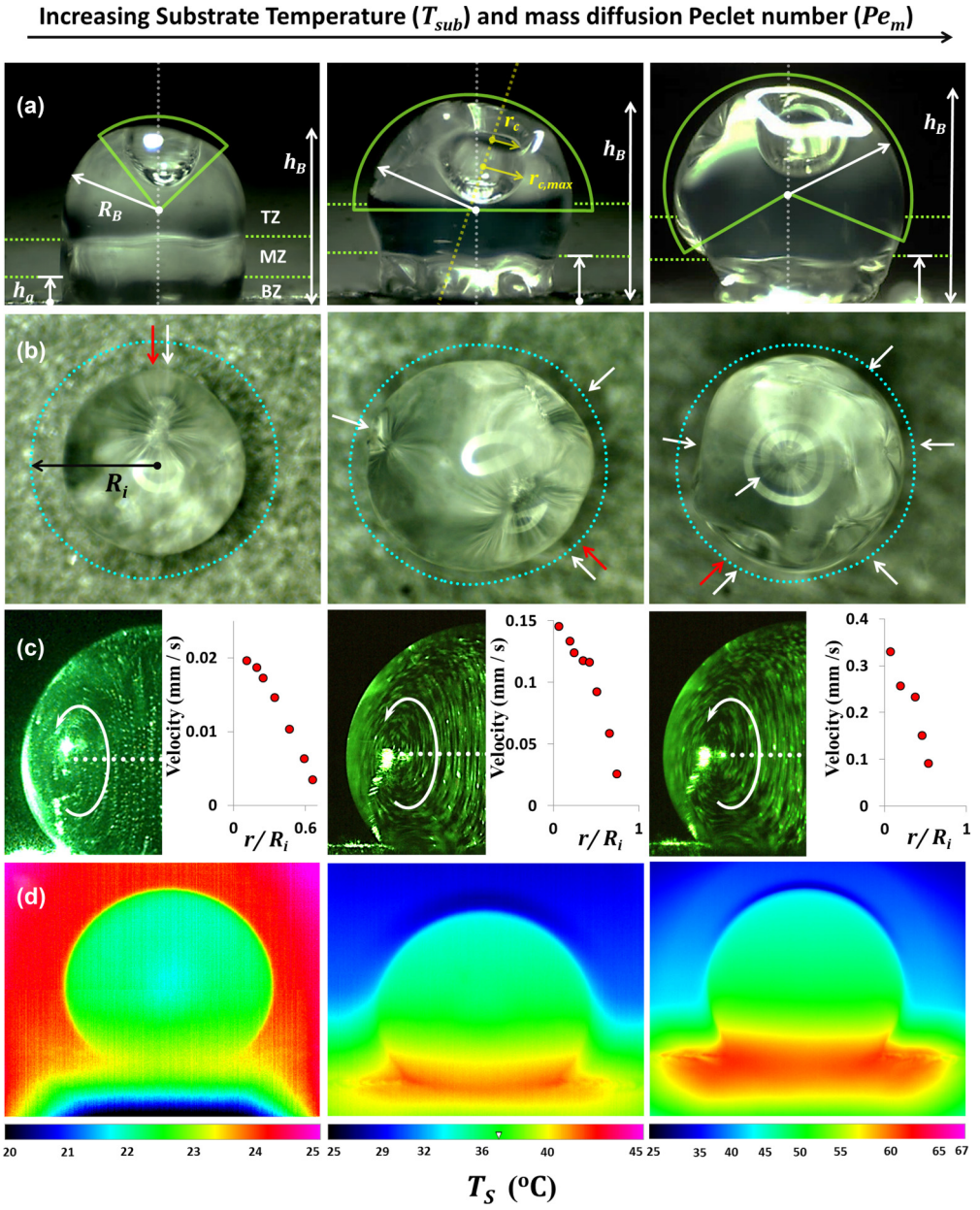

FIG. 2. Droplet morphology at different substrate temperatures (T_S) for initial concentration of 40 wt %. (a) Side view of the droplet; (b) top view of the droplet; (c) flow profiles inside the droplet with the radial variation in the velocity; (d) IR thermographs at different substrate temperatures. Blue dotted lines in (b) indicate the initial droplet size. White arrows represent the buckling locations while red arrows represent the rupturing sites. In (a), TZ, MZ, and BZ mean top zone, middle zone, and bottom zone, respectively. Scale bars equal 0.6 mm. Time instants for the images are 212, 150, and 77 s in first row and 116, 119, and 35 s in second row.

site only. It is worth noting that the buckling sites for all cases appear in the top half of the droplet away from the substrate. The aforementioned variations in the droplet structures due to increase in the substrate temperature at different PLRs are explained in detail in the following sections. In Sec. IV A, the internal liquid phase recirculation pattern has been studied. The Sec. IV B details the particle agglomeration, and in Sec. IV C and Sec. IV D, we explain shell formation and buckling (and subsequent rupturing) dynamics, respectively, while in Sec. IV E the universal nature of the growth of the daughter cavity (subsequent to rupturing) has been described.

IV. RESULTS AND DISCUSSION

A. Flow dynamics in a droplet

Figure 2 shows the temperature variation along the droplet height at different substrate temperatures (T_S). Subsequent to deployment, the droplet gains heat from the substrate through conduction leading to an increase in temperature near the base (Fig. 2). The apex (polar region) of the droplet, on the other hand, being away from the substrate (heating source), exhibits a comparatively lower temperature (Fig. 2, Table I). The apex temperature is further depressed due to the combined action of evaporative cooling and heat loss

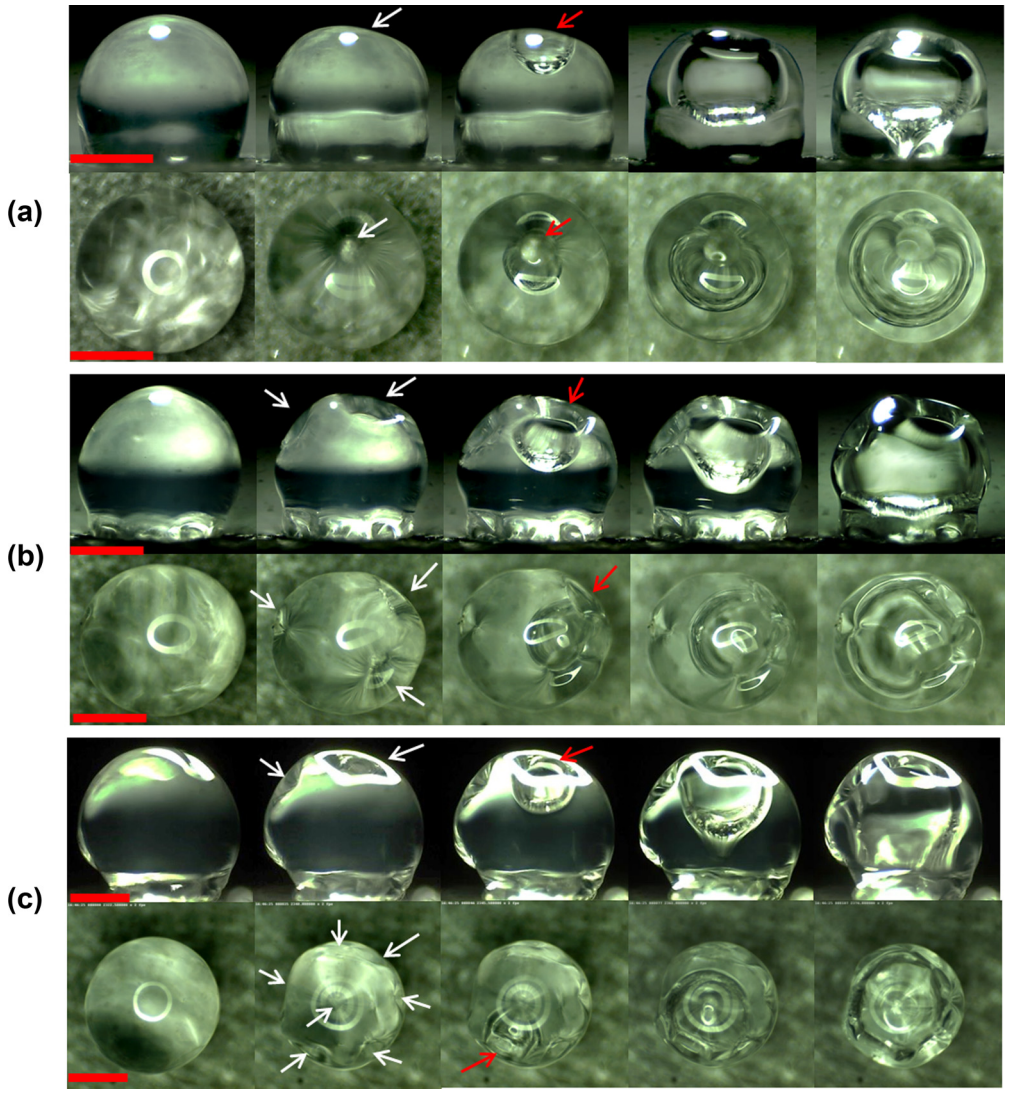

FIG. 3. Buckling front dynamics at substrate temperatures of (a) 25 °C, (b) 45 °C, and (c) 65 °C for initial concentration of 40 wt %. First row of each subsection represents the side view and second row shows the top view of the droplet. White arrows and red arrows denote the buckling and rupturing sites, respectively. Scale bars equal 0.6 mm. Time instants for the images are (a) 1, 116, 212, 320, and 442 s; (b) 1, 119, 150, 178, and 261 s; (c) 1, 35, 77, 86, and 107 s.

to the ambient from the droplet surface. Even though the vaporization rate is higher near the base (more latent heat), the effect of evaporative cooling is negated by the continuous supply of heat from the substrate. This longitudinal variation in temperature along the height leads to density stratification inside the droplet ($\Delta\rho = \rho_{\text{base}} - \rho_{\text{apex}}$ in Table I). It should be noted that even for a naturally drying droplet (unheated substrate), there exists a small temperature variation along the droplet height. In the absence of any heating source, the temperature gradient in a naturally drying droplet on a hydrophobic substrate is solely due to evaporative cooling (Fig. 2). Since the vaporization is suppressed near the three phase contact line for the naturally drying case [14], the interface temperature due to evaporative cooling is higher in the bottom half as compared to the upper half of the droplet. This creates a detectable density gradient leading to an internal recirculating liquid flow (Fig. 2). With increase in substrate temperature, this density gradient steepens (Table I) which in turn causes an increase in the internal recirculation velocity. In order to confirm that the recirculation velocity indeed increases with substrate temperature, the poloidal flow is visualized by seeding the droplet with 1-μm neutrally buoyant (Stokes's number $\ll 1.1$) tracer particles. These tracer particles are illuminated at the central plane of the droplet

TABLE I. Temperature and density variations at different substrate temperatures.

Substrate temperature, T_S(deg C)	ΔT(deg C)	$\Delta\rho$ (kg/m^3)
25	1	0.229 42
30	3	0.8797
45	6	2.5188
55	10	5.094
65	13	6.153

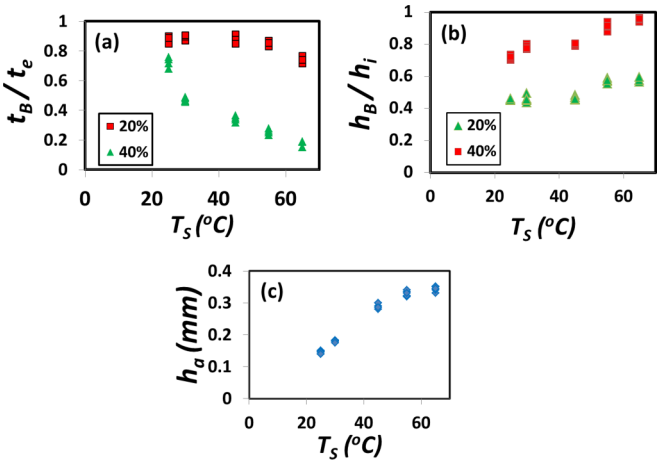

FIG. 4. (a) Normalized time delay to buckling onset for various T_S and concentrations; (b) normalized droplet height at buckling onset for initial particle loading rates of 20 and 40 wt %. at different T_S; (c) height of the agglomeration front at the droplet base at different substrate temperatures for $\varphi_o = 40$ wt %. Error is around ±3%–6%.

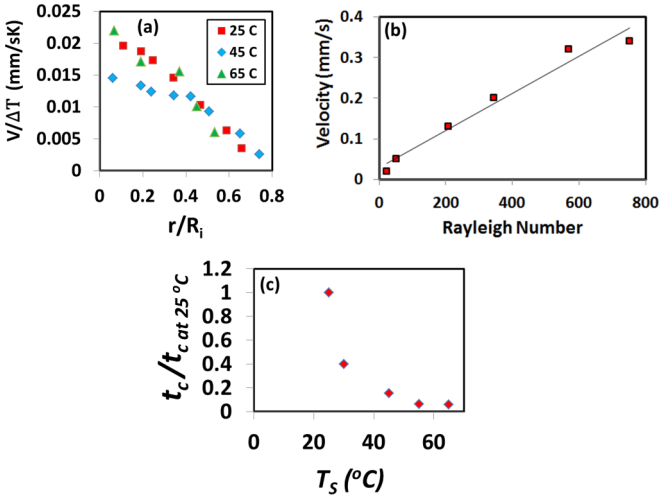

FIG. 5. (a) Radial variation of normalized velocity ($\Delta T = T_{\text{base}} - T_{\text{apex}}$); (b) increase in maximum velocity at different T_S with increase in Rayleigh number; (c) normalized time of churning (t_c) at different T_S for 40 wt %.

by a 170-μm-thick continuous laser sheet (Cobalt Samba 300 mW laser, $\lambda = 532$ nm) generated using a planoconvex and cylindrical lens arrangement. Recirculation velocity is approximated by tracking the seeder particles at various radial locations using short exposure images (3 fps: spatial resolution 22 µm/pixel). The characteristic flow profiles are illustrated in Fig. 2. Note that in the current work, velocity magnitudes of the internal flow are not quantitatively evaluated using particle image velocimetry (PIV). The flow pattern is only reported to showcase preferential particle transport due to the temperature induced flow field. However, estimations of the nominal velocity magnitude are undertaken to show the increase in velocity scale with substrate temperature (T_S). With increase in T_S from 25 °C to 65 °C, the recirculation velocity increases by an order (from ∼0.02 mm/s for 25 °C to ∼0.15 for 45 °C). It is, however, seen that the flow field remains similar in topology (toroidal recirculation pattern) for all substrate temperatures. Velocity is found to be maximum at the center of the droplet for all the cases with gradual decrease in the radial direction (Fig. 2). The velocity scales estimated from high speed images (at different substrate temperatures) are markedly close to the values reported by Dash *et al.* [13] based on two-dimensional PIV. The recirculatory motion of the flow inside the droplet can be either attributed to the Marangoni convection due to surface tension variation (surface tension of liquid decreases with temperature) or due to the buoyancy induced convection (resulting from density stratification) [13]. Ristenpart *et al.* [28] reported that if the ratio of thermal conductivity of the substrate (k_s) and droplet liquid (k_l), $k_R = \frac{k_s}{k_l} < 1.45$ and the base of the droplet is coldest, then the Marangoni flow would exhibit a similar pattern as shown in Fig. 2. However, in the current work even though $k_R = \frac{k_{\text{GDL}}}{k_{\text{water}}} \approx 0.76$,, the flow cannot be Marangoni convection due to the fact that the contact line of the droplet is at a higher temperature compared to the apex as can be seen from Fig. 2. As the interface temperature is higher near the substrate, the warmer fluid rises from the base towards the apex where it cools down and subsequently reverses its direction, thus creating a poloidal recirculation pattern. For droplets on a hydrophilic substrate, the vaporization rate is not suppressed near the three phase contact line. Hence, there is no occurrence of any density gradient. However, for a pinned contact line (for droplets on a hydrophilic substrate), the internal liquid flow pattern is very different [1] and is directed radially outwards (towards the contact line). Figure 5(b) shows the linear relationship between the flow velocity and Rayleigh number (also shown earlier by Dash *et al.* [13]), Ra $= \frac{\rho g \beta \Delta T L^3}{\mu \alpha}$, where ρ is the density, β is the thermal expansion of liquid, μ is the dynamic viscosity, α is the thermal diffusivity, and $\Delta T = T_{\text{base}} - T_{\text{apex}}$. This supplements the argument that the flow field inside the droplet is buoyancy driven. The fact that the flow field looks similar is further corroborated by the trend of the velocity profiles [as shown in Fig. 5(a), at different substrate temperatures] when normalized by the corresponding temperature differences (ΔT as explained above).

B. Droplet vaporization

According to Evans *et al.* [14], for a droplet drying under ambient conditions on a hydrophobic substrate, a region of high relative humidity (RH) builds up near the three phase contact line, which leads to a decrease in the evaporation flux close to the substrate. However, for droplets on a heated substrate, high temperature (implying high saturation pressure) ensures faster evaporation near the base compared to the upper section of the droplet ($\frac{J_{e_1}}{J_{e_2}} = 1.7$, where subscripts 1 and 2 refer to the upper and lower sections as marked in Fig. 6). Evaporation rate J_e is given by [26]

$$J_e \approx \frac{1}{n_L k_B T} \frac{D_v [p_s(T) - p_\infty]}{L}, \tag{1}$$

where n_L is the number density of water molecules, k_B is the Boltzmann's constant, L is the diffusion length scale, D_v is the air-water diffusion coefficient, and p_s is the saturation pressure

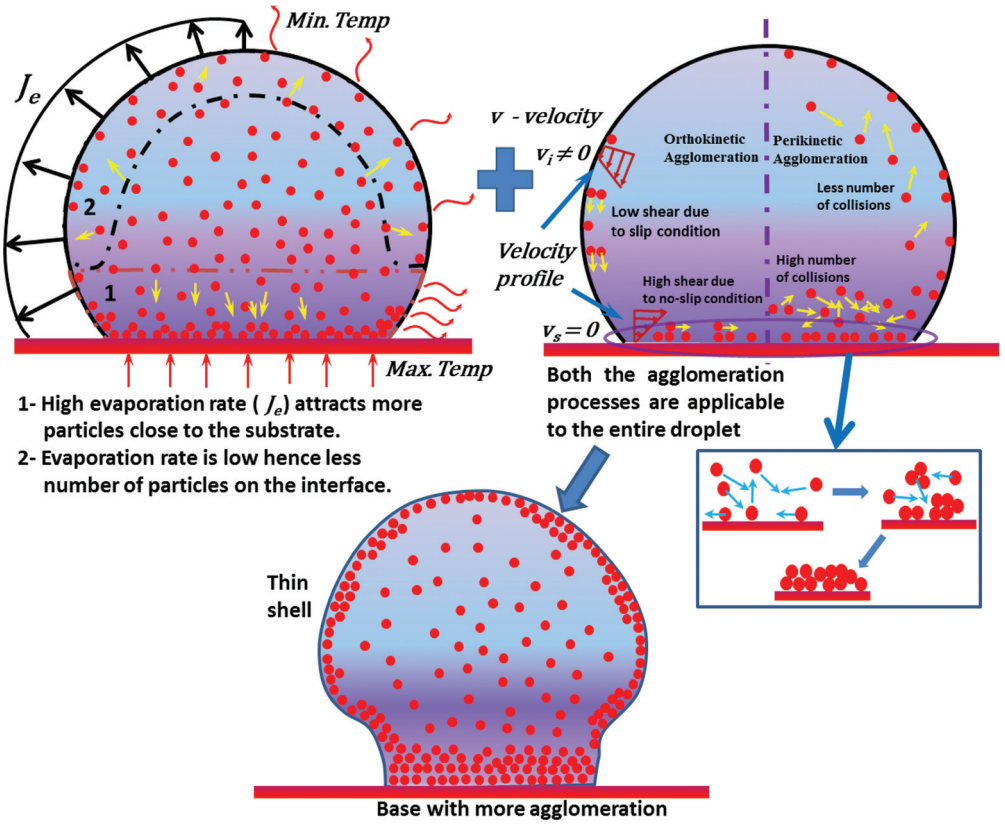

FIG. 6. Schematic showing the particle agglomeration due to different mechanisms. Droplet shown in the top left corner has two distinct regions of particle agglomeration defined by the dashed lines. Region 1 is close to the substrate and region 2 is close to the droplet periphery.

of water vapor (function of the droplet surface temperature), while p_∞ is the partial pressure of water vapor in the far field.

Thus, as the droplet evaporation progresses, more particles are transported close to the substrate ($\frac{N_1}{N_2} = 12$; subscripts 1 and 2 henceforth refer to regions 1 and 2 as marked in Fig. 6) where N is the particle number density (Fig. 6). Here, for order estimation of N_1, base thickness (at point of buckling) is considered. N_2 is estimated by considering the shell thickness as 10 μm (at which the shell buckles). The packing fraction of particles is assumed to be 0.6 for both estimates. This implies higher particle population near the three phase contact line and, consequently, there is a decrease in the number of particles in the upper half of the droplet for any given substrate temperature. Furthermore, the evaporation rate also increases substantially with increase in T_S ($\frac{J_{e65C}}{J_{e25C}} \approx 7$) as shown in Fig. 7(c) leading to increased concentration of particles near the base ($\frac{N_{1_{65C}}}{N_{1_{25C}}} = 2.43$) with enhancement in substrate temperature.

1. Particle agglomeration dynamics

Near the substrate and in the upper region of the droplet, the nanoparticles start to agglomerate forming larger clumps due to orthokinetic and perikinetic mechanisms as shown in Fig. 6. Smoluchowski [29] derived the expressions for perikinetic and orthokinetic agglomerations based on Brownian motion and flow shear rate (hydrodynamic interactions), respectively, as explained in the following subsections.

(a) Perikinetic agglomeration. Following Refs. [29–33], the perikinetic agglomeration rate is given by

$$J_{pk} \propto \frac{4kT N_i N_j}{3\mu}, \tag{2}$$

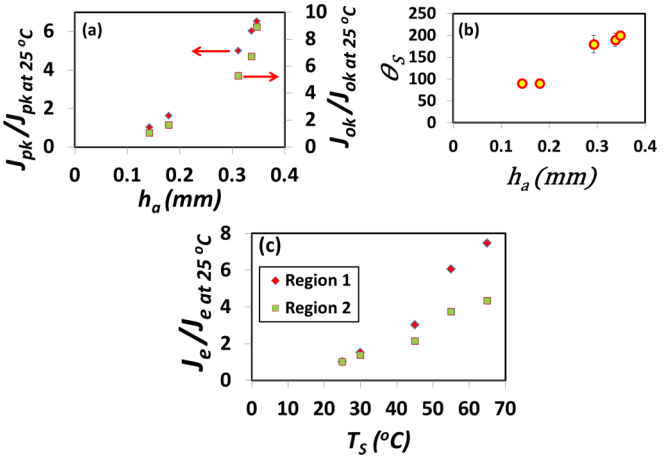

FIG. 7. (a) Normalized perikinetic and orthokinetic agglomeration rates. [Legend same as (c). Here regions 1 and 2 in (c) refer to sections marked in Fig. 6.] (b) Angle of the sector in which probable buckling sites are found for different base agglomeration heights (temperature dependent). (c) Normalized rate of evaporation at different T_S. All the graphs are for initial PLR of 40 wt %. Error is around ±2%−5%.

where μ is the dynamic viscosity, T is the temperature; N_i, N_j are the particle concentrations of type "i" and "j," respectively; and k is Boltzmann's constant. Smoluchowski [29] derived this rate considering the collision resulting from diffusive flux of particles (ith and jth particles; diffusion coefficient given by Stokes-Einstein equation) towards each other. Perikinetic agglomeration hence results from Brownian motion which increases sharply with temperature [34–36]. Perikinetic aggregation hence is particularly dominant for nanosized particles. The functional dependence shown in Eq. (2) has been well established both numerically as well as experimentally (in bulk) by many research groups [29–33]. However, in the context of evaporating nanoparticle-laden droplets, *in situ* experimental determination of the agglomeration rate is difficult since standard techniques like dynamic light scattering (DLS) cannot be used to the best of the authors' knowledge. However, it can be safely assumed that a similar function form [Eq. (2)] can be also used in the droplet framework.

The perikinetic aggregation rate is higher in region 1 due to the temperature being higher closer to the substrate ($\frac{J_{pk_1}}{J_{pk_2}} = 4.1$). It also increases with enhancement in T_S ($\frac{J_{pk,65\,^\circ C}}{J_{pk,25\,^\circ C}} \approx 1.1$) (for simplification, N_i and N_j are considered to be the same for calculating J_{pk} and J_{ok} (defined later) as shown in Fig. 7(a). Thus the particle agglomeration rate (due to particle collisions and shear interactions between them) is faster (compared to natural drying) resulting in a thicker agglomeration front [h_a in Figs. 2 and 4(c)] at the base of the droplet ($\frac{h_{a,65\,^\circ C}}{h_{a,25\,^\circ C}} = 2.43$). It can be seen from Fig. 4(c) that the base height increases with enhanced substrate heating.

(b) Orthokinetic agglomeration. Orthokinetic (shear driven) agglomeration rate is given in Refs. [29–32],

$$J_{ok} \propto \frac{2\dot{\gamma} d^3 N_i N_j}{3}, \tag{3}$$

where $\dot{\gamma}$ is the velocity gradient and d is the particle diameter. This expression was also derived by Smoluchowski [29] considering collisions of particles (ith and jth) moving along different streamlines in a given flow field. The functional dependence as proposed in Eq. (3) has been well validated in many experimental and numerical studies [36–40]. For example, the experimental work of [40] has shown that J_{ok} indeed increases linearly with shear rate. This experiment was done in the bulk phase in a stirred tank using different rotation speeds, hence creating low to high velocity gradients (shear). In order to check the same qualitatively, we carried out sample fluorescence studies in hydrophilic droplets (easier to diagnose) laden with micron sized (~900 nm) markers. We found that with temperature, the velocity increases leading to enhanced shear which further leads to increased particle accumulation/agglomeration. In the current experiment, we have shown previously that with temperature (25 °C – 45 °C), flow velocity and shear increases by an order (Fig. 2). This conclusively proves that temperature plays a dominant role in enhancing orthokinetic agglomeration rate.

Thus, comparing the shear rate near the substrate and in the upper half, we get

$$\frac{du_1}{d\delta}(\sim 0.7\,\mathrm{s}^{-1}) > \frac{du_2}{d\delta}, \tag{4}$$

where u_1,u_2 are fluid velocities in sections 1 and 2 (Fig. 6), respectively, and δ is the boundary layer thickness which is assumed to be around 0.1 mm. This is due to the no slip applicable in region 1 (due to substrate). In region 2 (Fig. 6) the velocity is not zero at the liquid-air interface. Thus, orthokinetic agglomeration is faster near the substrate (region 1) as compared to region 2 as shown in Fig. 6. At the same time, the orthokinetic agglomeration rate in region 1 increases substantially with the increase in T_S ($\frac{du_{65\,^\circ C}}{d\delta} > \frac{du_{25\,^\circ C}}{d\delta}$ or $\frac{J_{ok_{65\,^\circ C}}}{J_{ok_{25\,^\circ C}}} = 8.8$) [Fig. 7(a)].

As shown in the inset in Fig. 6, individual particles combine together to form aggregates of different sizes. These clusters can be defined as i-fold aggregates where i denotes the number of particles forming the cluster. These clusters grow (increase in i-fold) with time forming microscale aggregate networks.

(c) Growth of aggregates. The growth of aggregates can be further explained by using the population balance equation [29–33] given by

$$\frac{\partial N(i,t)}{\partial t} = \frac{1}{2}\int_0^i \beta(j,i-j,t)N(j,t)N(i-j,t)dj - \int_0^\infty \beta(i,j,t)N(i,t)N(j,t)dj. \tag{5}$$

Here, the left side of the Eq. (5) represents the temporal change of i-fold aggregates. The first term on the right side shows the generation of i-fold aggregates due to collision of smaller clusters and the second term represents the depletion of i-fold aggregates to form larger aggregates. $\beta[\sim\frac{4\dot{\gamma}}{3}(a_i + a_j)^3$ for orthokinetic and $\sim\frac{2kT}{3\mu}\frac{(a_i+a_j)^2}{a_i a_j}$ for perikinetic] (where a_i and a_j are the particles sizes) is called the collision frequency and is a function of the shear rate ($\frac{du}{d\delta}$) and temperature (T). Hence, larger number of collisions (due to higher temperature) and high shear rate leads to formation of larger aggregates at the base at a rapid rate (depletion of lower order or smaller sized aggregates). As the aggregate size increases (micron order), orthokinetic aggregation becomes dominant [41].

It is to be noted that formal solution of Eqs. (2)–(5) is beyond the scope of the current work. Equations (2)–(5) have been used qualitatively to corroborate the experimental trends as observed in Figs. 2 and 3.

C. Shell formation

The process of shell formation can be defined using a nondimensional parameter termed the Peclet number, $\mathrm{Pe} = \frac{R_i^2/D_a}{t_e}$ (where D_a is the particle diffusion coefficient calculated using the Stokes-Einstein equation and t_e is the time taken for complete evaporation) which is found to be in the range of $20 < \mathrm{Pe} < 220$. $\mathrm{Pe} \gg 1$ signifies that the rate of diffusion is one order lower than the rate of evaporation; i.e., the drying process is fast enough for shell formation.

Under natural drying, due to faster evaporation from the upper half of the droplet, more NPs agglomerate at the periphery of the droplet by perikinetic and orthokinetic aggregation [17]. Near the north pole, there is a decrease in the particle agglomeration because of flow divergence leading to a weak soft spot [17]. This shell near the polar region subsequently buckles under capillary pressure as explained in the next section.

However, for a droplet drying on a heated substrate, there is a decrease in the quantity of particles available for peripheral shell formation due to the formation of a thicker base agglomeration front (AF; h_a) (as explained in the previous sections). Assuming spherical nanoparticles of uniform diameter of 22 nm, a rough estimate of the decrease in the number density of NPs in region 2 (Fig. 6) can be determined and when compared to the naturally drying droplet is found to be $\frac{N_{65\,^\circ\mathrm{C}}}{N_{25\,^\circ\mathrm{C}}} \approx 0.6$ at buckling onset. Also, increased height and radius of the heated droplet result in larger surface area ($\frac{S_{65\,^\circ\mathrm{C}}}{S_{25\,^\circ\mathrm{C}}} \approx 1.75$ where S is the surface area of the droplet at the buckling onset) available for particle deposition. Thus the number density of NPs decreases by 45% due to increase in surface temperature from 25 °C to 65 °C.

Figure 5(c) shows the variation in normalized churning time ($t_c = \frac{v_{\max}}{h_i}$, $v_{\max}$ is the maximum flow velocity, and h_i is the initial height of the droplet) at different substrate temperatures. Churning time here is defined as the time taken by the particle from the top of the droplet to reach the substrate. There is a substantial decrease in t_c at high T_S which shows that there is vigorous dispersion of particles in the upper half of the droplet. Such churning of particles leads to more uniform agglomeration in a spatial sense throughout the upper sector of the droplet. This degree of homogenization increases with increase in temperature (higher $v_{\max}$). Uniform agglomeration implies uniform but thinner shell (compared to natural drying) formation. The shell thus formed exhibits reduced thickness over a large spherical sector (Figs. 2 and 6) around the top half rather than the polar region.

Faster particle agglomeration rate (at higher substrate temperature) throughout the droplet (for all heated cases) leads to an early formation of the dome structure (Fig. 2) which in turn reduces the time delay to buckling onset as shown in Fig. 4(a) ($\frac{t_{b,65\,^\circ\mathrm{C}}}{t_{b,25\,^\circ\mathrm{C}}} \approx 0.019$ for PLR of 40 wt %). Due to early dome formation, the increase in droplet radius ratio is only marginal; i.e., $\frac{R_c}{R_B} \approx 0.8$. Due to the reduction in evaporation rate in the lower sector for a naturally drying droplet, time delay to buckling onset is significantly higher than the heated case and thus the contact radius to meridian radius ratio becomes $\frac{R_c}{R_B} \approx 1$ from the initial $\frac{R_c}{R_i} \approx 0.73$ (R_c is the contact radius of the droplet; R_B is the meridian radius at buckling onset). This is also evident from the rate of decrease of the droplet dimension ($\frac{dR}{dt} \sim 0.006$ at 25 °C increases to $\frac{dR}{dt} \sim 0.01$ at 65 °C; contact radius, however, remains the same). There is also significant increase (∼40%−50%) in the normalized height of the droplet (at buckling onset) with increase in surface temperature for both PLRs as can be seen from Fig. 4(b). However, irrespective of φ_o and T_S, at the onset of buckling, there is no further decrease in the droplet dimensions; i.e., the aspect ratio of the droplet $AR_B = \frac{h_B}{2R_B}$ becomes constant.

D. Buckling characteristics

In the case of natural drying, the evaporation and subsequent shell formation is a slow process which leads to an inhomogeneous shell with minimum thickness around the apex region, gradually increasing in thickness towards the base [17]. This shell subsequently buckles at a critical capillary pressure at a *single site* near the apex (pole) which is the weakest soft spot, i.e., the site with minimum shell thickness [17]. Subsequently this buckled shell ruptures, thereby leading to the formation of a daughter cavity [17]. Note that under natural drying cases (20T25 and 40T25), the shell buckling and rupture is observed only at a *single site* which exists in a narrow spherical sector encompassing the north pole (Fig. 2). In contrast, for substrate heating, the droplet deformation (for initial PLR of 40 wt %) is characterized by *multiple buckling sites* that can form at any location in the upper dome structure. The shell rupture and daughter cavity growth, however, still occurs from only one of these buckling sites. These distinct features are illustrated in Figs. 2 and 3.

For heated cases, since thin and more homogeneous shells are formed (as explained in the previous section), there is no preferential location for buckling as in the case of natural drying. This indicates that multiple weak soft spots can exist over a larger spatial extent rather than just the polar region. Figure 7(b) shows the average variations in the angle of this sector (in which buckling sites are expected) as a function of base agglomeration height which in turn is a function of T_S; hence, $\frac{\theta_{s,65\,^\circ\mathrm{C}}}{\theta_{s,25\,^\circ\mathrm{C}}} \approx 2$. The number of buckling sites and spherical sector angle increases with increase in base height (h_a). It is clear [Figs. 2 and 4(c)] that temperature increase thickens the base region and thins out the peripheral shell thickness, leading to increased probability of buckling at multiple points over progressively larger spherical sectors [Fig. 7(b)]. It is estimated that the shell thickness required for buckling scales as O (12 μm) [15]. These (thin shell and multiple buckling points) are also evident in the final precipitate as shown in Figs. 8 and 9. Furthermore, to confirm that multiple buckling sites are not due to the porous nature of the substrate or substrate roughness, experiments were done on a poly dimethyl sulphate (PDMS) substrate with surface roughness of ∼10 nm. Droplets ($\varphi_o = 40$ wt %) dispensed on PDMS substrate also show buckling from multiple locations when the substrate is heated to the same temperatures as in the current work.

This phenomenon of multiple buckling is, however, not observed in the case of $\phi_o = 20$ wt %. According to Sadek *et al.* [42], a viscous shell is formed on the surface of the droplet when the initial concentration ϕ_o reaches the critical concentration ϕ_c. As can be seen from Fig. 4(a), there is a considerable increase in time delay to buckling onset as ϕ_o is decreased from 40 to 20 wt % ($\frac{t_{b,40\%}}{t_{b,20\%}} \approx 6$ for 65 °C) since more water needs to be evaporated from the droplet to attain ϕ_c. This leads to significant decrease in h_B for $\phi_o = 20$ wt % ($\frac{h_B}{h_i} \approx 0.6$ at $T_S = 65$ °C) as compared to 40 wt % ($\frac{h_B}{h_i} \approx 0.9$ at $T_S = 65$ °C) with very little increase in R_B. Thus for PLR of 20 wt %, there is not much increase in the surface area of the droplet available for particle agglomeration (as in the case of 40 wt %) ($\frac{S_{65\,^\circ\mathrm{C}}}{S_{25\,^\circ\mathrm{C}}} \approx 1.4$) with increase in T_S. This leads to shell formation similar to the natural case

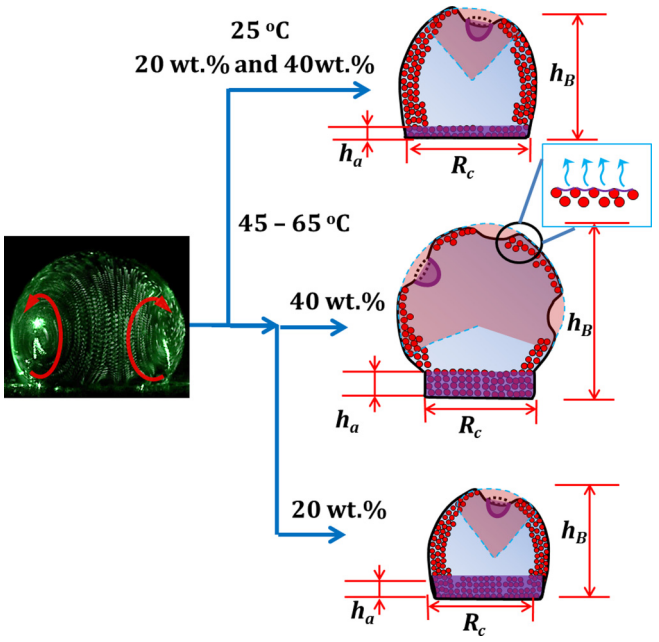

FIG. 8. Summary of the buckling dynamics for heated and nonheated droplets for different PLRs.

with a single weak soft spot at the north pole of the droplet ($\frac{\theta_{s,65\,^\circ\mathrm{C}}}{\theta_{s,25\,^\circ\mathrm{C}}} \approx 1$). A schematic showing the buckling locations and angle sector variations for initial PLRs of 20 and 40 wt % for both natural and hated cases is illustrated in Fig. 8.

Even though the shell buckles from multiple locations (for PLR of 40 wt %), only one of these sites leads to rupturing resulting in the formation of a cavity. As explained by Pauchard *et al.* [16], a given shell ruptures when the stress due to stretching of the shell overcomes the Van der Waals force of attraction between the particles. Thus, among the multiple buckled sites, the one with the maximum stretched shell (minimum thickness) ruptures to create a millimeter scale hole. Thus, the rupturing of the buckled cavity [primary cavity (PC)] causes a substantial decrease in the capillary pressure at the punctured site. Then, as per the invasion percolation theory [43,44], air enters the ruptured hole (capillary pressure being minimum at that location) forming a cavity [daughter cavity (DC)] inside the droplet.

For both natural and heated substrate configurations, a stratified varying density core forms inside the droplet which can be demarcated into three zones, namely, top (TZ), middle (MZ), and bottom zone (BZ), as shown in Fig. 2. As reported by Bansal *et al.* [17], the daughter cavity growth through these zones is governed by solvent evaporation across the droplet surface. Therefore, with increase in T_S the rate of cavity expansion [both longitudinally ($\frac{dy}{dt}$) and radially ($\frac{dr}{dt}$)] is expected to increase significantly (higher surface temperature of the droplet promotes faster evaporation rate). For instance, in the natural case, the cavity grows in tandem in both the lateral and longitudinal directions in the TZ whereas in the MZ, $\dot{y} > \dot{r}$. On the other hand, for the heated case, in the TZ, the cavity expands faster in the longitudinal direction compared to the radial direction; i.e., $\dot{y} > \dot{r}$ ($\dot{y} \approx 0.05\,\mathrm{mm\,s^{-1}}$ and $\dot{r} \approx 0.02\,\mathrm{mm\,s^{-1}}$) while it expands in tandem in the MZ, $\dot{y} \approx \dot{r} \approx 0.01\,\mathrm{mm\,s^{-1}}$. There is a decrease in the DC growth rate in MZ as it is more viscous compared to the TZ. As the cavity reaches the BZ in the natural case, it expands through it and sometimes may continue all the way to the bottom puncturing a hole through the bottom surface. However, for the heated case, the BZ consists of a thicker AF as stated above and thus restricts the further expansion of the cavity in the BZ as can be seen in Figs. 3 and 9.

E. Universal cavity growth

The methodology for cavity volume calculation has been reported in Bansal *et al.* [17] based on which the rate of change of the cavity volume (V_{DC}) is given by

$$\frac{dV_{\mathrm{DC}}}{dt} \approx JS\varepsilon, \tag{6}$$

where V_{DC} is the volume daughter cavity, S is the surface area of the droplet (S increases with increase in T_S), ε is the porosity of the particle packing on the droplet surface, and J is the rate of solvent evaporation per unit area which is a function of the difference in partial pressure as defined in Eq. (1). From Eq. (1), J can also be written as

$$J = \frac{J'}{L}, \tag{7}$$

where $J' \approx \frac{1}{n_L k_B T} D_v[p_s(T) - p_\infty]$ is a constant with respect to ϕ_o (for a given T_S). Simplifying Eqs. (6) and (7), by considering the initial cavity volume $V_{\mathrm{DC}} = 0$ at $t = 0$,

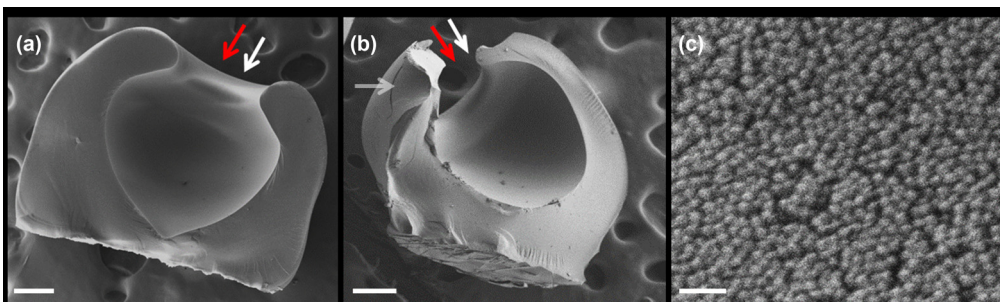

FIG. 9. SEM images showing the final precipitate (for 40 wt %) for substrate temperatures of (a) 25 °C; (b) 45 °C. (c) Nanoparticle packing on the droplet surface. White and red arrows denote the buckling and rupturing sites, respectively. Scale bars on (a) and (b) equal 200 μm and on (c) equal 100 nm.

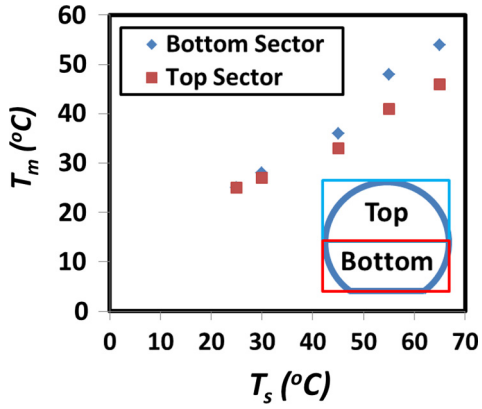

FIG. 10. Mean temperature in the top and bottom sectors of the droplet at different substrate temperatures.

we get

$$V_{\mathrm{DC}} = S\varepsilon \frac{J'}{L} t. \tag{8}$$

According to Eq. (7), J' is a function of the surface temperature (inversely proportional) and saturation pressure of the water vapor near the droplet surface (directly proportional). Thus, J' increases with T_S as the change in saturation pressure $[p_s(T)]$ is greater than the change in surface temperature (since saturation vapor pressure of water increases exponentially with temperature). However, to simplify the calculations, the droplet is divided into two sectors (top and bottom) at the middle as shown in Fig. 10 (inset). Mean temperatures of the two sectors are determined (Fig. 10). J' is calculated separately for the two sectors by considering the partial pressure values at the mean surface temperature. Similarly, the droplet surface area is calculated separately for each sector. Hence the normalization factor now becomes $\frac{\epsilon}{L}(S_T J'_T + S_B J'_B)t_m$ where subscripts T and B refer to top and bottom sectors of the droplet as shown in Fig. 10. In the heated case, t_m is the time from the onset of puncturing until the end of complete DC growth while for the natural case t_m is the time elapsed between the onset of puncturing and DC expansion in MZ. Bansal *et al.* [17] considered the porosity and diffusion length to be 0.4 [considering closely packed particles as shown in Fig. 9(c)] and 0.2 mm (final average shell thickness), respectively. For all heated substrate cases, particle packing in the final dried precipitate is similar to the natural drying case (i.e., random close packing) [Fig. 9(c)] and the final shell thickness is found to be $\sim O$ (0.2 mm) [Fig. 9(b)]. Hence, adopting a similar ratio ($\frac{\epsilon}{L} = 2000$), the cavity volume V_{DC} is normalized by the aforementioned factor. The normalized volume is plotted against the normalized time (t/t_m) as shown in Fig. 11, in which all the curves irrespective of initial particle loading rate and substrate temperatures collapse into a universal trend. Thus, it is clear from Fig. 11 that the cavity growth is indeed universal in nature since when compared with the plots of absolute volume daughter cavity (inset in Fig. 11), the collapse of the data resulting in a universal trend seems to be a valid argument. The cavity growth is supported by the evaporation from the droplet surface through the porous shell.

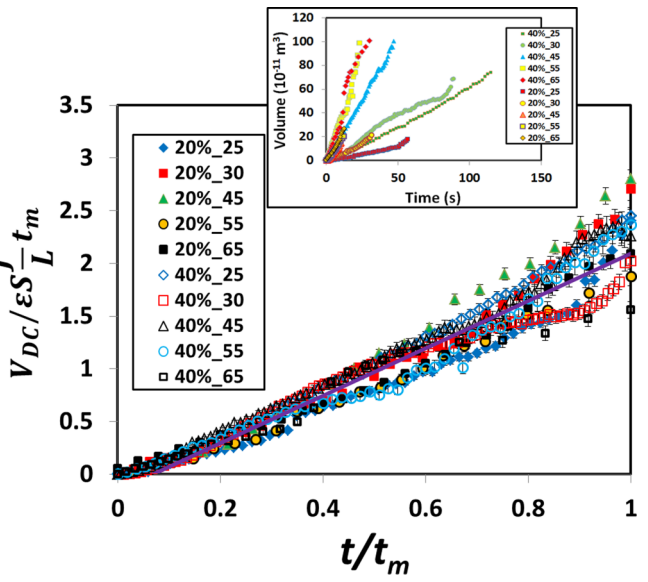

FIG. 11. Universal variation of normalized daughter cavity volume with time at different nanoparticle concentrations and substrate temperatures ($SJ' = S_T J'_T + S_B J'_B$). Inset shows the plots of absolute volume of daughter cavities. Error is around $\pm 2\%-5\%$.

The observed scatter in data around the mean line is due to two reasons: Firstly, to calculate the volume of the cavity, we have assumed the cavity to be of a particular shape depending on its aspect ratio as reported by Bansal *et al.* [17]. However, as can be seen from Fig. 3, the actual cavity profile deviates (from actual experiments) from the assumed geometries. The larger deviations from the mean are observed only in the latter part of the curve ($t/t_m > 0.6$, i.e., in the middle zone) as shown in Fig. 11, since, as the cavity enters the middle zone, its growth tends to be random and its shape tends to distort. Thus, due to the aforementioned conditions, it is difficult to get the exact cavity contour which leads to error in the cavity volume calculation. This error is subsequently reflected in the normalized volume graph. Secondly, it is difficult to predict the dynamic variation in the porosity value (ε). This can also be responsible for the scatter in the data around the mean line.

Thus, using the above relation, daughter cavity expansion can be predicted with prior knowledge of the droplet aspect ratio and substrate temperature.

V. CONCLUSION

Evaporation characteristics of nanoparticle-laden droplets placed on heated substrates are experimentally studied for two different PLRs of 20 and 40 wt %. Heating the nanoparticle-laden sessile droplet initiates a chain of events leading to significant changes in the droplet morphology. The morphological transitions are primarily due to the combined action of evaporation, agglomeration, and internal liquid flow. Liquid phase velocity profiles are found to be buoyancy driven due to a differential temperature gradient along the droplet surface. The recirculation patterns estimated for various substrate temperatures were found to be similar in topology although the velocity magnitude increases by one order. The final precipitate

morphology is a strong function of substrate temperature. The most significant effect of droplet heating is the increase in the number of buckling sites with increasing surface temperature for a PLR of 40 wt %. However, droplets with lower concentration of 20 wt % still buckled from a single location only. Buckled droplets for all cases undergo rupturing, forming daughter cavities. The cavity volume when normalized by droplet surface area and evaporative flux follows a universal trend irrespective of temperature and initial PLR. This further conclusively proves that the daughter cavity expansion inside the droplet is indeed driven by solvent vaporization from the droplet.

ACKNOWLEDGMENT

Funding from Department of Science and Technology is gratefully acknowledged.

All authors contributed equally to this work.

[1] R. D. Deegan, O. Bakajin, T. F. Dupont, G. Huber, S. R. Nagel, and T. A. Witten, Nature (London) **389**, 827 (1997).
[2] J. Jing, J. Reed, J. Huang, X. Hu, V. Clarke, J. Edington, D. Housman, T. S. Anantharaman, E. J. Huff, B. Mishra, B. Porter, A. Shenker, E. Wolfson, C. Hiort, R. Kantor, C. Aston, and D. C. Schwartz, Proc. Natl. Acad. Sci. USA **95**, 8046 (1998).
[3] Q. Li, Y. T. Zhu, I. A. Kinloch, and A. H. Windle, J. Phys. Chem. B **110**, 13926 (2006).
[4] T. Lim, S. Han, J. Chung, J. T. Chung, S. Ko, and C. P. Grigoropoulos, Int. J. Heat Mass Transfer **52**, 431 (2009).
[5] M. Singh, H. M. Haverinen, P. Dhagat, and G. E. Jabbour, Adv. Mater. **22**, 67 (2010).
[6] W. Xu, R. Leeladhar, Y.-T. Tsai, E.-H. Yang, and C.-H. Choi, Appl. Phys. Lett. **98**, 073101 (2011).
[7] M. Maeki, H. Yamaguchi, K. Yamashita, H. Nakamura, M. Miyazaki, and H. Maeda, Chem. Commun. **48**, 5037 (2012).
[8] P. Jiang, J. F. Bertone, K. S. Hwang, and V. L. Colvin, Chem. Mater. **11**, 2132 (1999).
[9] E. Rabani, D. R. Reichman, P. L. Geissler, and L. E. Brus, Nature (London) **426**, 271 (2003).
[10] S. Narayanan, J. Wang, and X. M. Lin, Phys. Rev. Lett. **93**, 135503 (2004).
[11] M. Schnall-Levin, E. Lauga, and M. P. Brenner, Langmuir **22**, 4547 (2006).
[12] H. Hu and R. G. J. Larson, Phys. Chem. B **110**, 7090 (2006).
[13] S. Dash, A. Chandramohan, J. A. Weibel, and S. V. Garimella, Phys. Rev. E **90**, 062407 (2014).
[14] L. Chen and J. R. G. Evans, Langmuir Lett. **25**, 11299 (2009).
[15] A. Miglani and S. Basu, Soft Matter **11**, 2268 (2015).
[16] F. Boulogne, F. Giorgiutti-Dauphiné, and L. Pauchard, Soft Matter **9**, 750 (2013).
[17] L. Bansal, A. Miglani, and S. Basu, Phys. Rev. E **92**, 042304 (2015).
[18] Y. Zhang, S. Yang, L. Chen, and J. R. G. Evans, Langmuir **24**, 3752 (2008).
[19] C. H. Chon, S. Paik, J. B. Tipton, and K. D. Kihm, Langmuir **23**, 2953 (2007).
[20] Z. Lin and S. J. Granick, Am. Chem. Soc. **127**, 2816 (2005).
[21] K. Mougin and H. Haidara, Langmuir **18**, 9566 (2002).
[22] Y. O. Popov and T. A. Witten, Phys. Rev. E **68**, 036306 (2003).
[23] L. Pauchard and Y. Couder, Europhys. Lett. **66**, 667 (2004).
[24] J. Paulose and D. R. Nelson, Soft Matter **9**, 8227 (2013).
[25] B. Sobac and D. Brutin, Colloids Surf., A **448**, 34 (2014).
[26] N. Tsapis, E. R. Dufresne, S. S. Sinha, C. S. Riera, J. W. Hutchinson, L. Mahadevan, and D. A. Weitz, Phys. Rev. Lett. **94**, 018302 (2005).
[27] S. Dash and S. V. Garimella, Phys. Rev. E **89**, 042402 (2014).
[28] W. D. Ristenpart, P. G. Kim, C. Domingues, J. Wan, and H. A. Stone, Phys. Rev. Lett. **99**, 234502 (2007).
[29] M. Z. Smoluchowski, Z. Phys. Chem. **92**, 129 (1917).
[30] Y. Gan and L. Qiao, Int. J. Heat Mass Transfer **54**, 4913 (2011).
[31] L. G. Bremer, P. Walstra, and T. V. Vliet, Colloids Surf., A **99**, 121 (1995).
[32] C. S. O'Brien, Ph.D. thesis, University of South Florida, 2003.
[33] B. Pathak, P. Deepu, S. Basu, and R. Kumar, Int. J. Heat Mass Transfer **59**, 161 (2013).
[34] *Kinetics of Aggregation and Gelation*, edited by F. Family and D. P. Landau (North-Holland, Amsterdam, 1984).
[35] *On Growth and Form*, edited by H. E. Stanley and N. Ostrowski (Nijhoff, Dordrecht, 1986).
[36] *The Scientific Bases of Flocculation*, edited by K. J. Ives (Sijthoff and Noordhoff, Alphen aan den Rijn, Netherlands, 1978).
[37] K. Higashitani, S. Miyafusa, T. Matsuda, and Y. J. Matsuno, Colloid Interface Sci. **77**, 21 (1980).
[38] J. Gregory, Chem. Eng. Sci. **36**, 1789 (1981).
[39] S. Hansen and J. M. Ottino, J. Colloid Interface Sci. **179**, 89 (1996).
[40] P. T. Spicer, W. Keller, and S. E. Pratsinis, J. Colloid Interface Sci. **184**, 112 (1996).
[41] M. Peltomaki, Cluster-cluster aggregation in an external field in two dimensions, Ph.D. thesis, Helsinki University of Technology, Department of Engineering Physics and Mathematics, 2002.
[42] C. Sadek, P. Schuck, Y. Fallourd, N. Le Pradeau, C. Floch-Fouéré, and R. Jeantet, Dairy Sci. & Technol. **95**, 771 (2015).
[43] D. Wilkinson and J. F. Willemsen, J. Phys. A: Math. Gen. **16**, 3365 (1983).
[44] M. Prat, Int. J. Multiphase Flow **19**, 691 (1993).